Surface bound waves and optical interactions in excitonic thin films

EUNSONGYI LEE, BYUNG HOON WOO, IN CHEOL SEO, SOO-CHAN AN, AND YOUNG CHUL JUN*

School of Materials Science and Engineering, Ulsan National Institute of Science and Technology (UNIST), Ulsan 44919, South Korea
*ycjun@unist.ac.kr

Abstract: Excitonic films such as J-aggregate-doped polymer films can exhibit sharp Lorentzian dispersions and thus have various optical features in the visible region. They can even show an optically metallic response and can be considered as alternative plasmonic materials. However, there were no systematic studies on optical interactions in such excitonic films. Here, we perform theoretical investigations on optical modes and interactions in planar excitonic thin films. We gradually vary the dye concentration and the film thickness and study optical coupling to surface bound waves (surface polariton modes and epsilon-near-zero modes). We also investigate thin-film interferences in high-loss and low-loss regimes. Finally, we discuss the freespace impedance matching that can result from the Lorentzian dispersion in excitonic films. Our work enables in-depth understandings on optical interactions in excitonic films and it can provide guidelines for various nanophotonic applications in the visible region.

References and links

1. J. A. Schuller, E. S. Barnard, W. Cai, Y. C. Jun, J. S. White, and M. L. Brongersma, "Plasmonics for extreme light concentration and manipulation," Nat. Mater. **9**(3), 193–204 (2010).
2. G. V. Naik, V. M. Shalaev, and A. Boltasseva, "Alternative plasmonic materials: beyond gold and silver," Adv. Mater. **25**(24), 3264–3294 (2013).
3. S. K. Saikin, A. Eisfeld, S. Valleau, and A. Aspuru-Guzik, "Photonics meets excitonics: natural and artificial molecular aggregates," Nanophotonics **2**(1), 21–38 (2013).
4. B. J. Walker, A. Dorn, V. Bulović, and M. G. Bawendi, "Color-selective photocurrent enhancement in coupled J-aggregate/nanowires formed in solution," Nano Lett. **11**(7), 2655–2659 (2011).
5. J. Bellessa, C. Bonnand, J. C. Plenet, and J. Mugnier, "Strong coupling between surface plasmons and excitons in an organic semiconductor," Phys. Rev. Lett. **93**(3), 036404 (2004).
6. E. Eizner, O. Avayu, R. Ditcovski, and T. Ellenbogen, "Aluminum nanoantenna complexes for strong coupling between excitons and localized surface plasmons," Nano Lett. **15**(9), 6215–6221 (2015).
7. G. Zengin, M. Wersäll, S. Nilsson, T. J. Antosiewicz, M. Käll, and T. Shegai, "Realizing strong light-matter interactions between single nanoparticle plasmons and molecular excitons at ambient conditions," Phys. Rev. Lett. **114**(15), 157401 (2015).
8. S. Balci, B. Kucukoz, O. Balci, A. Karatay, C. Kocabas, and G. Yaglioglu, "Tunable plexcitonic nanoparticles: a model system for studying plasmon-exciton interaction from the weak to the ultrastrong coupling regime," ACS Photonics **3**(11), 2010–2016 (2016).
9. M. J. Gentile, S. Núñez-Sánchez, and W. L. Barnes, "Optical field-enhancement and subwavelength field-confinement using excitonic nanostructures," Nano Lett. **14**(5), 2339–2344 (2014).
10. B. H. Woo, I. C. Seo, E. Lee, S. Y. Kim, T. Y. Kim, S. C. Lim, H. Y. Jeong, C. K. Hwangbo, and Y. C. Jun, "Dispersion control of excitonic thin films for tailored superabsorption in the visible region," ACS Photonics **4**(5), 1138–1145 (2017).
11. M. S. Bradley, J. R. Tischler, and V. Bulović, "Layer-by-layer J-aggregate thin films with a peak absorption constant of 10^6 cm^{-1}," Adv. Mater. **17**(15), 1881–1886 (2005).
12. L. Gu, J. Livenere, G. Zhu, E. E. Narimanov, and M. A. Noginov, "Quest for organic plasmonics," Appl. Phys. Lett. **103**(2), 021104 (2013).
13. A. Cacciola, C. Triolo, O. D. Stefano, A. Genco, M. Mazzeo, R. Saija, S. Patanè, and S. Savasta, "Subdiffraction light concentration by J-aggregate nanostructures," ACS Photonics **2**(7), 971–979 (2015).
14. J. R. Tischler, M. S. Bradley, V. Bulović, J. H. Song, and A. Nurmikko, "Strong Coupling in a Microcavity LED," Phys. Rev. Lett. **95**(3), 036401 (2005).

15. Y. Sugawara, T. A. Kelf, J. J. Baumberg, M. E. Abdelsalam, and P. N. Bartlett, "Strong coupling between localized plasmons and organic excitons in metal nanovoids," Phys. Rev. Lett. **97**(26), 266808 (2006).
16. N. T. Fofang, T.-H. Park, O. Neumann, N. A. Mirin, P. Nordlander, and N. J. Halas, "Plexcitonic nanoparticles: plasmon-exciton coupling in nanoshell-J-aggregate complexes," Nano Lett. **8**(10), 3481–3487 (2008).
17. É. Boulais, N. P. D. Sawaya, R. Veneziano, A. Andreoni, J. L. Banal, T. Kondo, S. Mandal, S. Lin, G. S. Schlau-Cohen, N. W. Woodbury, H. Yan, A. Aspuru-Guzik, and M. Bathe, "Programmed coherent coupling in a synthetic DNA-based excitonic circuit," Nat. Mater. **17**(2), 159–166 (2017).
18. Y. U. Lee, E. Garoni, H. Kita, K. Kamada, B. H. Woo, Y. C. Jun, S. M. Chae, H. J. Kim, K. J. Lee, S. Yoon, E. Choi, F. Mathevet, I. Ozerov, J. C. Ribierre, J. W. Wu, and A. D'Aléo, "Strong nonlinear optical response in the visible spectral range with epsilon-near-zero organic thin films," Adv. Opt. Mater. **6**(14), 1701400 (2018).
19. B. H. Woo, I. C. Seo, E. Lee, S.-C. An, H. Y. Jeong, and Y. C. Jun, "Angle-dependent optical perfect absorption and enhanced photoluminescence in excitonic thin films," Opt. Express **25**(23), 28619–28629 (2017).
20. J. D. Caldwell, L. Lindsay, V. Giannini, I. Vurgaftman, T. L. Reinecke, S. A. Maier, and O. J. Glembocki, "Low-loss, infrared and terahertz nanophotonics with surface phonon polaritons," Nanophotonics **4**(1), 44–68 (2015).
21. J. L. Bricks, Y. L. Slominskii, I. D. Panas, and A. P. Demchenko, "Fluorescent J-aggregates of cyanine dyes: basic research and applications review," Methods Appl. Fluoresc. **6**(1), 012001 (2017).
22. B. Ding, M. Qiu, and R. J. Blaikie, "Manipulating light absorption in dye-doped dielectric films on reflecting surfaces," Opt. Express **22**(21), 25965–25975 (2014).
23. B. E. A. Saleh and M. C. Teich, *Fundamentals of Photonics* (John Wiley & Sons, 2007), Chap.7.
24. H. Raether, *Surface Plasmons on Smooth and Rough Surfaces and on Gratings* (Springer, 1988).
25. S. Vassant, J.-P. Hugonin, F. Marquier, and J.-J. Greffet, "Berreman mode and epsilon near zero mode," Opt. Express **20**(21), 23971–23977 (2012).
26. Y. C. Jun, J. Reno, T. Ribaudo, E. Shaner, J.-J. Greffet, S. Vassant, F. Marquier, M. Sinclair, and I. Brener, "Epsilon-Near-Zero Strong Coupling in Metamaterial-Semiconductor Hybrid Structures," Nano Lett. **13**(11), 5391–5396 (2013).
27. S. Campione, I. Brener, and F. Marquier, "Theory of epsilon-near-zero modes in ultrathin films," Phys. Rev. B **91**(12), 121408 (2015).
28. D. W. Berreman, "Infrared absorption at longitudinal optic frequency in cubic crystal films," Phys. Rev. **130**(6), 2193–2198 (1963).
29. M. Schubert, *Infrared Ellipsometry on Semiconductor Layer Structures* (Springer, 2004).
30. P. Yeh, *Optical Waves in Layered Media* (John Wiley & Sons, 2005) pp. 83–99, 150–151.
31. M. A. Kats and F. Capasso, "Optical absorbers based on strong interference in ultra-thin films," Laser Photonics Rev. **10**(5), 735–749 (2016).
32. S. Collin, "Nanostructure arrays in free-space: optical properties and applications," Rep. Prog. Phys. **77**(12), 126402 (2014).
33. H. A. Haus, *Waves and Fields in Optoelectronics* (Prentice-Hall, 1983).

1. Introduction

Plasmonic nanostructures can enable the extreme confinement and manipulation of light at deep-subwavelength scales [1]. A myriad of nanoscale optical components and devices have been proposed based on surface plasmons in metal nanostructures. However, such metal nanostructures suffer from intrinsic ohmic losses and often have limitations in applications. In this regard, various alternative materials for plasmonics have been studied [2].

Certain organic molecules such as J-aggregates have strong excitonic responses in the visible range [3–13]. In fact, J-aggregate dyes have been well-known in the photonics community for strong coupling and dye-sensitizer studies [5,14–16]. Exciton transport in J-aggregates was also considered for excitonic circuits that can enable control of optical energy transport at the molecular level [17]. Because of the large oscillator strength, J-aggregate films can show an optically metallic response (Re[ε] < 0) in the visible region. Therefore, they can support excitonic surface polariton (SP) modes [9–13], similar to surface plasmon polaritons in metals or surface phonon polaritons in polar materials. Moreover, it is found that J-aggregate films show a large nonlinear optical enhancement in the visible region at the epsilon-near-zero (ENZ) wavelength (Re[ε] ~0) [18]. They have also been employed for perfect absorber studies recently [10,19]. The excitonic absorption line in J-aggregates can be tuned over the whole visible region by changing monomer design [3,4], and thus these materials could be useful for various nanophotonic studies in the visible region.

These excitonic films show sharp Lorentzian dispersions in the visible region and thus can have various optical features. By varying the dye concentration in a polymer film, we can

realize both optically metallic and non-metallic films. However, there were no detailed studies on the optical properties of excitonic thin films. Here, we conduct systematic theoretical investigations on optical interactions in planar excitonic thin films. We study optical modes and interferences in excitonic films with gradually varying dye concentration and film thickness. Because organic films are commonly prepared by a solution process, both dye concentration and film thickness can be easily controlled (see, for example, Ref [10,18]. for experimental conditions). The dye concentration can be varied by adjusting the weight percent of a dye and a polymer matrix in solution. And the film thickness can be controlled by the spincoating speed or solution concentration. We first study surface bound waves (SP and ENZ modes) in the attenuated total reflection (ATR) configuration. Then, we consider thin-film interferences in high-loss and low-loss regions in both ATR and air-incidence conditions. Finally, we discuss the freespace impedance matching that can be realized in excitonic films. Our analyses and in-depth investigations given here can provide valuable guidelines for various nanophotonic applications based on excitonic films.
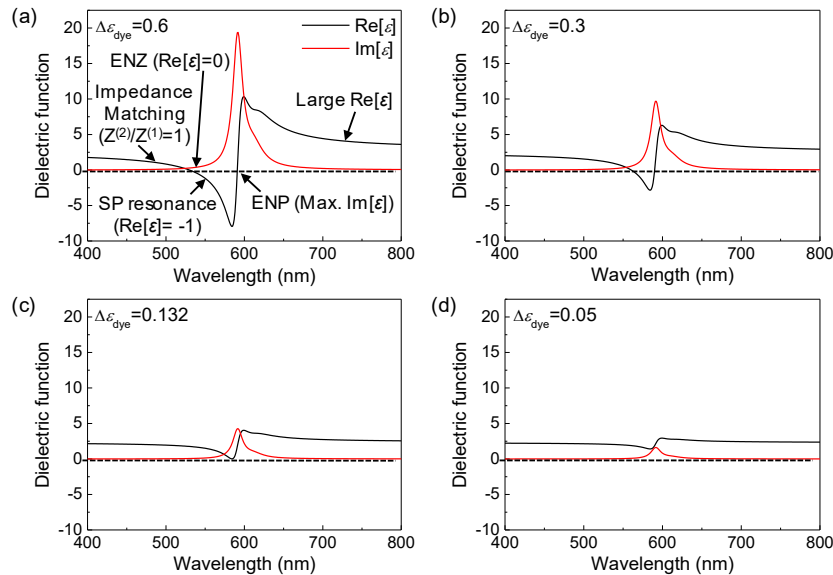

Fig. 1. The dielectric function of excitonic thin films with varying $\Delta\varepsilon_{dye}$ (Black curve: $Re[\varepsilon]$, Red curve: $Im[\varepsilon]$). (a) $\Delta\varepsilon_{dye}$ is 0.6, which shows metallic characteristics. The dispersion exhibits various features in the visible region: epsilon-near-zero (ENZ) point (~530 nm) (where $Re[\varepsilon]$ is zero), surface polariton (SP) resonance wavelength (where $Re[\varepsilon] = -1$), epsilon-near-pole (ENP) position (around which $Im[\varepsilon]$ possesses a maximum value), impedance matching point (where $Z^{(2)}/Z^{(1)} = 1$). $Z^{(2)}$ and $Z^{(1)}$ are the characteristic impedance of the excitonic film and the incident medium, respectively. (b) $\Delta\varepsilon_{dye}$ is 0.3. (c) $\Delta\varepsilon_{dye}$ is 0.132. The variation in the dielectric function is small and $Re[\varepsilon]$ is nonzero over the whole spectrum. (d) $\Delta\varepsilon_{dye}$ is very small, 0.05. (c) and (d) correspond to a nonmetallic case.

2. Modeling of the dielectric constants in excitonic thin films

Several polar dielectric materials (such as SiC and hBN) have strong phonon resonances in the infrared region [20]. These materials can have sharp Lorentzian dispersions with the negative permittivity region and have been widely used in the studies of surface phonon polaritons. However, these phonon resonances are usually located in the infrared region, and the phonon frequency is a fixed material property and thus not tunable. Excitonic films can have the similar Lorentzian dispersion relation in the visible region that can result in optically metallic responses ($Re[\varepsilon] < 0$). Excitonic resonances in J-aggregate thin films can be tunable over the whole visible

region by modifying the monomer design. Therefore, excitonic films could be a very useful platform for nano-optical studies in the visible region.

In this work, we consider a cyanine dye (such as TDBC) [21] mixed with a polymer matrix (poly vinyl alcohol, PVA). The dielectric constants of this excitonic film can be described using the Lorentz model [9,22]:

$$\varepsilon_{\mathrm{ext}}(\omega) = \varepsilon_{\mathrm{PVA}} + \Delta\varepsilon_{\mathrm{dye}} \sum_i A_i \frac{\omega_i^2}{\omega_i^2 - \omega^2 - i\omega\gamma_i}, \tag{1}$$

where $\varepsilon_{\mathrm{PVA}} = 2.26$ is the dielectric constant of PVA and the weighting factor A_i satisfies $\sum_i A_i = 1$. We use the relevant parameters available in literature for two-oscillator Lorentz fitting ($i = 0, 1$) [9]: $\omega_0 = 2.10$ eV, $\gamma_0 = 0.053$ eV, $f_0 = 0.36$, $\omega_1 = 2.03$ eV, $\gamma_1 = 0.0988$ eV, and $f_1 = 0.10$, where f_i is the reduced oscillator strength $f_i = \Delta\varepsilon_{\mathrm{dye}} \cdot A_i$. We introduced the parameter $\Delta\varepsilon_{\mathrm{dye}}$ to explicitly show the dye concentration dependence in the Lorentz model. From Eq. (1), we note that the maximum (or the peak value) of Im[ε] $\sim \Delta\varepsilon_{\mathrm{dye}} \cdot A_0 \omega_0 / \gamma_0$. Because this peak value is determined by the dye concentration, we find that $\Delta\varepsilon_{\mathrm{dye}}$ is also directly related to the dye concentration. For a systematic investigation of optical properties in both metallic and non-metallic films, we consider the effect of varying dye concentrations in a polymer matrix. In this regard, we gradually vary $\Delta\varepsilon_{\mathrm{dye}}$ from 0.6 (optically metallic) to 0.05 (non-metallic) and investigate the optical responses of excitonic films.

Figure 1 shows the real and imaginary parts of the dielectric constants for different $\Delta\varepsilon_{\mathrm{dye}}$ values. The excitonic film with $\Delta\varepsilon_{\mathrm{dye}} = 0.6$ shows a clear metallic response; the imaginary part of the dielectric constants (Im[ε]) has a sharp peak at the excitonic line (590 nm) and the real part has negative values (Re[ε] < 0) in the wavelength region shorter than the excitonic line. This optically metallic behavior can be understood from the Kramers-Kronig relation. When there is a strong absorption peak, it should be highly dispersive too. When the imaginary part is very large because of strong absorption, the real part fluctuates significantly and it can be negative. This metallic response has a finite bandwidth, and the film becomes a normal dielectric (Re[ε] > 0) away from the metallic region. This metallic film can exhibit various optical features in the visible range, as indicated in Fig. 1(a); excitonic surface polaritons (SPs), epsilon-near-zero (ENZ) (Re[ε] $\sim$0), epsilon-near-pole (ENP) (Im[ε] $\sim$peak), freespace impedance matching ($Z^{(2)}/Z^{(1)} \sim$1), and large-ε region. Figure 1 also shows a weakly metallic case (Fig. 1(b)) and non-metallic ones (Fig. 1(c),(d)). As $\Delta\varepsilon_{\mathrm{dye}}$ decreases, the Im[ε] peak value gradually decreases and the fluctuation of Re[ε] also decreases. Therefore, the excitonic film eventually becomes non-metallic.

3. Surface bound waves in the ATR configuration

We first consider the attenuated total reflection (ATR) configuration [glass/excitonic film/air] to study optical modes in excitonic films. The ATR configuration is often used to excite surface bound waves. The absorption (A) spectra of excitonic films were calculated by the transfer matrix method (TMM) [23]. The refractive indices of glass and air were assumed to be 1.5 and 1, respectively, and we obtained absorption by $A = 1 - R - T$ (R: reflection, T: transmission). Beyond the critical angle, the transmission is naturally suppressed ($T = 0$). Then, the absorption can reach near unity ($A \sim$1) when the reflection becomes zero ($R \sim$0).
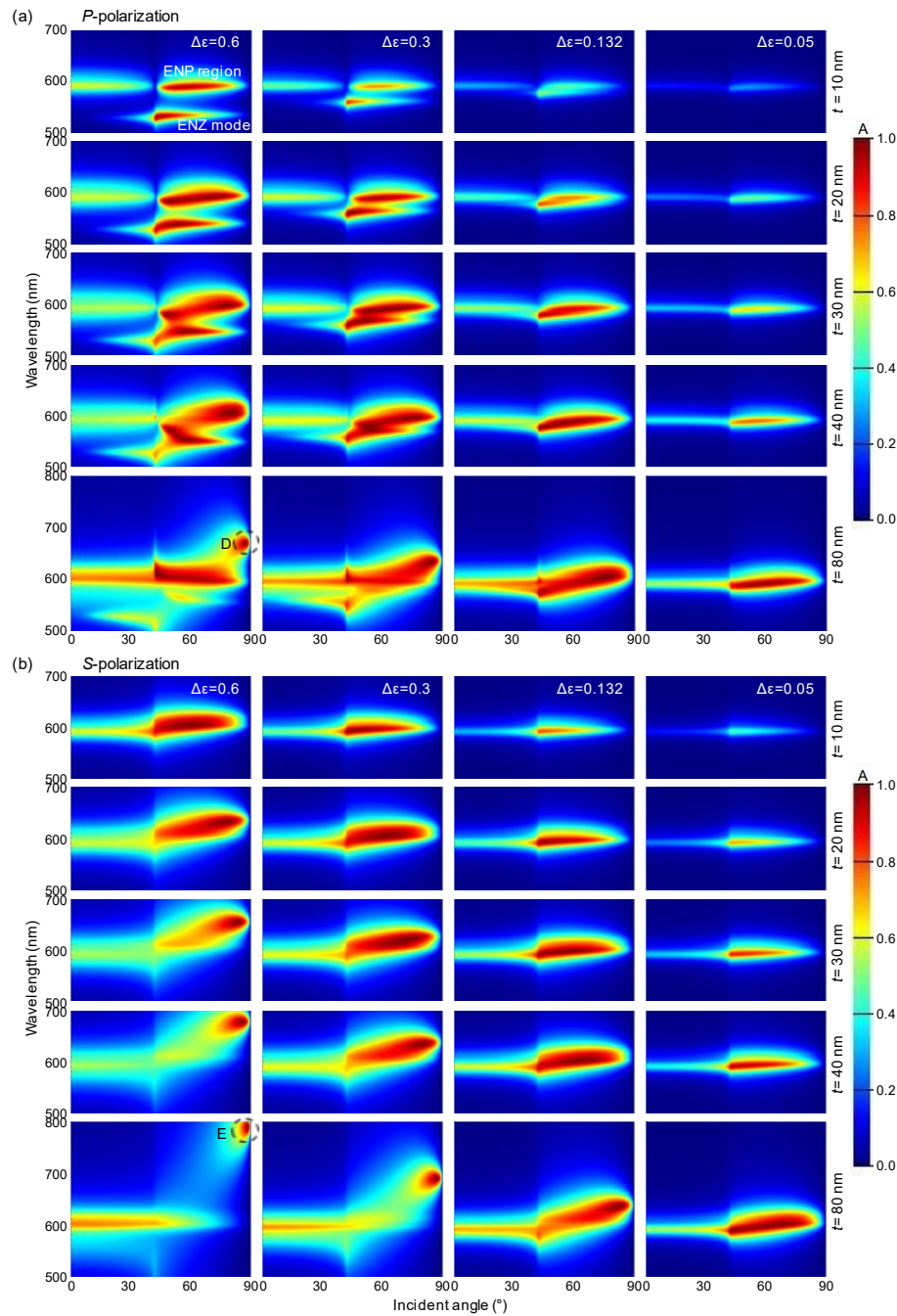
Fig. 2. Absorption map as a function of wavelength and incidence angle for different $\Delta\varepsilon_{dye}$ and film thickness t under ATR condition. (a) p-polarization and (b) s-polarization. Region D and E in the low-loss region are indicated by dotted circles in (a) and (b), respectively.

Figure 2 shows absorption colormaps for different $\Delta\varepsilon_{dye}$ values and film thicknesses ($t = 10$ ~80 nm). High absorption is represented in red color. We first explain general behavior in the absorption colormaps and then consider their physical origin. For a 10 nm-thick metallic film with $\Delta\varepsilon_{dye} = 0.6$ (Fig. 2(a)), there appear two strong absorption bands for p-polarization in ENP and ENZ regions. These absorption bands are almost flat over a wide range of incidence angle.

The vertical discontinuity at 42° corresponds to the critical angle (θ_c) at the glass/air interface. For thicker films, these absorption bands are not flat anymore and a clear wavelength-dependent dispersion appears. In addition, an isolated, strong absorption point appears at a very large incident angle (~80°). In the weakly metallic film ($\Delta\varepsilon_{dye} = 0.3$), we have a similar absorption map. However, the absorption band in the ENZ region moves to a longer wavelength region, because of the shifted ENZ wavelength (look at Fig. 1(b)). For smaller dye concentrations ($\Delta\varepsilon_{dye} = 0.132, 0.05$), the separate absorption band does not appear clearly, because the excitonic film becomes nonmetallic and the separate ENZ wavelength does not exist clearly in these cases [Figs. 1(c), 1(d)]. Only a single absorption band is present near the ENP region (i.e. high-loss region) in non-metallic films. For the s-polarization case, the absorption colormaps are simpler [Fig. 2(b)]; a strong absorption band appears mainly in the ENP region. An isolated, strong absorption point again exists at a large incidence angle, similar to the p-polarization case.

Now we consider the physical origin of the angle- and thickness-dependent optical features observed in Fig. 2. We consider the ATR configuration as shown in Fig. 3(a). Figures 3(b) and 3(c) show the absorption colormaps (p-polarization) for 50 nm and 20 nm thick metallic films ($\Delta\varepsilon_{dye} = 0.6$). The dispersion curve of the SP mode is shown together (olive curve). The SP mode dispersion is given by the following equation [24],

$$k_{\parallel} = \frac{\omega}{c}\sqrt{\frac{\varepsilon_{exc} \cdot \varepsilon_{air}}{\varepsilon_{exc} + \varepsilon_{air}}}, \tag{2}$$

where ω and c are the angular frequency and the speed of light. ε_{exc} and ε_{air} are the dielectric constants of the excitonic film and air ($\varepsilon_{air} = 1$). The in-plane momentum $k_{\parallel}$ is related to the incidence angle θ: $k_{\parallel} = \frac{\omega}{c}n_{glass}\sin\theta$. In the 50 nm thick film [Fig. 3(a)], strong light absorption in region A matches the SP dispersion curve and thus we find that light absorption occurs due to SP mode coupling. However, in the thinner film (20 nm thick), the absorption colormap looks very different although the dielectric constant of the film is the same. Now, the SP mode dispersion (solid olive curve) does not match the strong absorption band. Instead, we find that the absorption band follows the dispersion of another bound mode, called ENZ mode (region B) [25–27]. This mode exists for ultra-thin films and its dispersion curve lies close to the ENZ frequency. The dispersion relation for this p-polarized (or TM) mode can be obtained from the following analytic equation for a general three-layer system [25]:

$$\left(1 + \frac{\varepsilon_1 k_{z,3}}{\varepsilon_3 k_{z,1}}\right) = i\tan\left(k_{z,2}d\right)\left(\frac{\varepsilon_2 k_{z,3}}{\varepsilon_3 k_{z,2}} + \frac{\varepsilon_1 k_{z,2}}{\varepsilon_2 k_{z,1}}\right), \tag{3}$$

where $k_{z,p} = \left(\varepsilon_p \omega^2 / c^2 - k_{\parallel}^2\right)^{1/2}$, $p = 1,2,3$. By solving this equation, we can obtain dispersion curves around the ENZ frequency. From the dispersion relation, we can identify two branches [Fig. 3(f)]; one is a leaky mode (called Berreman mode [25,28,29]) on the left side of the light line, and the other a bound mode (ENZ mode) on the right side of the light line. When the film is very thin, the dispersion curves of both modes become flattened and get closer to the ENZ frequency (Re[$\varepsilon(\omega)$] ~0). We will consider the Berreman modes later in the air-incidence case. Here, we discuss the excitation of ENZ modes in the ATR configuration. The ENZ dispersion curves of the [glass/excitonic film/air] system are plotted on the absorption map in Fig. 3(c) (violet line). The bound ENZ mode can be considered as an extreme case of long-range (LR) surface plasmon polariton (SPP) modes. The electric field in the ENZ mode is strongly enhanced inside the film, following the boundary condition for the normal electric field component ($\varepsilon_1 E\perp_1 = \varepsilon_2 E\perp_2$). Note that $E\perp_1$ should diverge when ε_1 goes to zero (however, in real materials, the electric field remains finite due to nonzero optical losses or Im[ε]). As clearly

shown in Fig. 3, depending on the film thickness, incident light can be coupled to either a SPP mode or an ENZ mode.
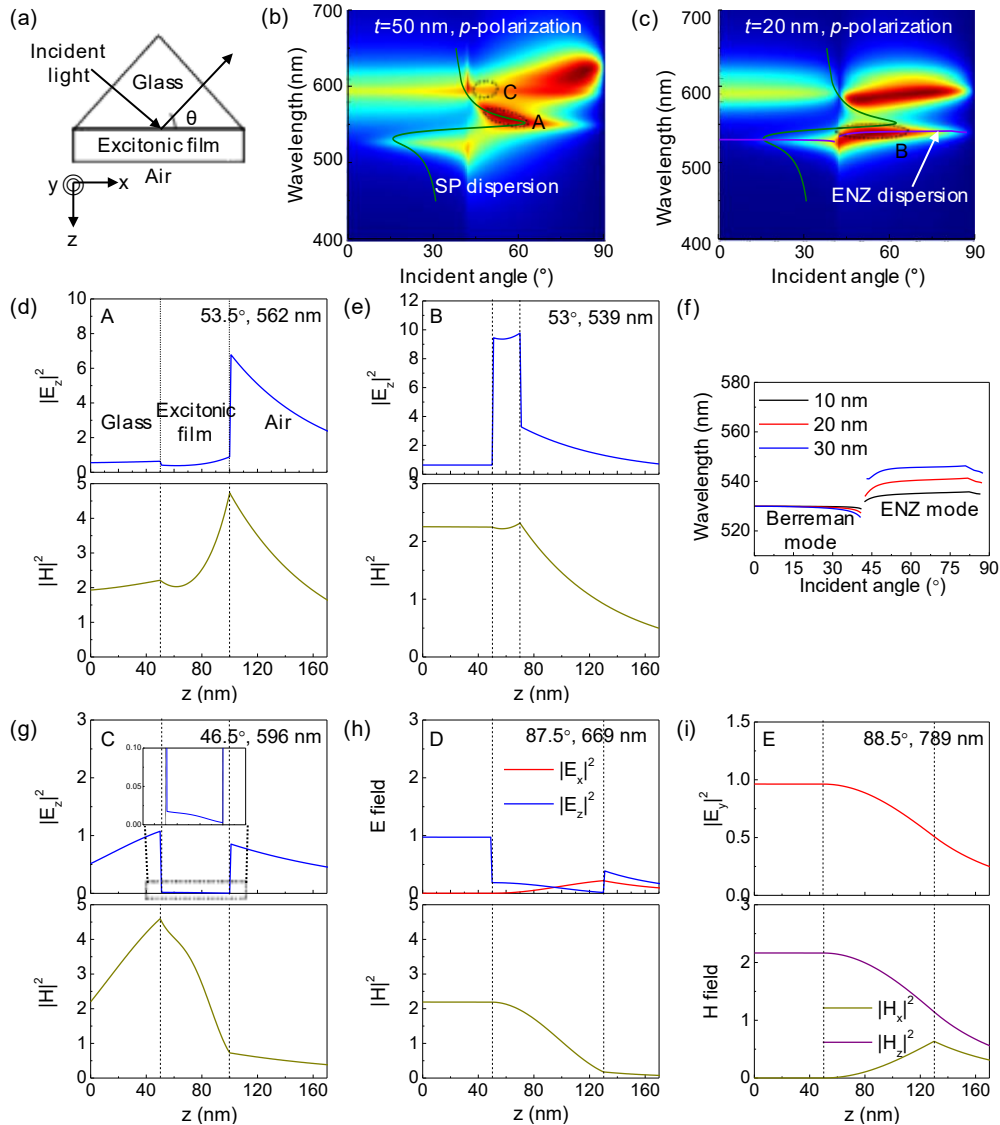

Fig. 3. (a) Schematic of the ATR condition. (b),(c) Absorption colormap together with the dispersion relation curve of SP (olive line) and ENZ (violet line) modes for 50 nm and 20 nm-thick films under *p*-polarization ($\Delta\varepsilon_{dye}$ = 0.6). (d),(e),(g)-(i) Electric (upper panel) and magnetic (lower panel) field profiles of the excitonic thin film for the ATR condition [glass/excitonic film/air structure]. Incident light comes from the glass. Each point corresponds to (d) region A and (g) region C in the absorption map of Fig. 3(b) with 50 nm-thick, (e) region B in the absorption map of Fig. 3(c) with 20 nm-thick. (h) Region D in the absorption map of Fig. 2(a) under *p*-polarization. (i) Region E in the absorption map of Fig. 2(b) under *s*-polarization. (f) Dispersion relation curve of ENZ modes for various thicknesses.

SP and ENZ modes also show different field profiles. The electric and magnetic field profiles in Figs. 3(d)-(e) are obtained from TMM calculations too. The field profile for the SP mode resembles that of the SP mode in a silver film. The magnetic field has a peak at the film/air interface and exponentially decays away from it, showing the feature of a surface bound

wave. The magnetic field in the ENZ mode also shows the similar bound way feature. However, in this case, the electric field (E_z) is strongly enhanced inside the film because of the boundary condition, as discussed above. In addition to bound SP and ENZ modes, we find that strong absorption can occur in either the high-loss (C) or low-loss (D, E) region. Near-perfect absorption in the high-loss (or ENP) region occurs rather over a wide range of incidence angles, while it occurs at a very large, grazing incidence angle in the low-loss region. The field profiles in the region C to D are also very different from those for surface bound waves. The magnetic field profiles show the feature of thin-film interferences, while the normal electric field component (E_z) in region C and D follows the boundary condition. The optical interactions in the high-loss (C) and low-loss (D, E) regions will be discussed further in the next section.

4. Thin film interferences in high-loss and low-loss regions

Excitonic films have both high-loss and low-loss wavelength regions because of the Lorentzian dispersion. The high-loss region occurs near the excitonic absorption line or ENP position (i.e. the peak of Im[ε]), while the low-loss region corresponds to the dielectric region away from this excitonic line. As shown in the colormap in Fig. 2, strong light absorption can occur in the either high-loss or low-loss region. It can be understood in terms of thin film interferences. We explain this using the phasor diagram of partial reflected waves. The complex reflection coefficient can be expressed as a sum of partial reflected wave [10,30],

$$r = \sum_{m=0}^{\infty} r_m = r_{12} + t_{12}t_{21} \sum_{m=1}^{\infty} r_{23}{}^m r_{21}{}^{m-1} e^{2mi\beta}, \qquad (4)$$

where r_m is the round trip reflection coefficient ($r_m = t_{12}t_{21}r_{23}{}^m r_{21}{}^{m-1} e^{2mi\beta}$ for $m \geq 1$, and $r_0 = r_{12}$) and $\beta = (2\pi/\lambda)\tilde{n}_2 d_2 \cos\theta$. r_{jk} and t_{jk} are the Fresnel reflection and transmission coefficients from medium j to medium k, given by $r_{jk} = (\tilde{Y}_j - \tilde{Y}_k)/(\tilde{Y}_j + \tilde{Y}_k)$ and $t_{jk} = 2\tilde{Y}_j/(\tilde{Y}_j + \tilde{Y}_k)$ with the admittance $\tilde{Y}_j = \tilde{n}_j/\cos\tilde{\theta}_j$ for p-polarization, $\tilde{Y}_j = \tilde{n}_j \cos\tilde{\theta}_j$ for s-polarization, and $\tilde{\theta}_j = \sin^{-1}(\sin\theta_1/\tilde{n}_j)$. This infinite series can be also summed up as follows (called Airy formula),

$$r = \frac{r_{12} + r_{23}\exp(i2\beta)}{1 + r_{12}r_{23}\exp(i2\beta)}. \qquad (5)$$

In the complex phasor diagram, two axes correspond to the real and imaginary components of the reflection coefficient. Arrows indicate partial reflected waves (r_0, r_1, r_2, …) and they are connected together head-to-tail. At near-zero reflection (or near-perfect absorption, $A = 1 - R = 1$), the connected phasor arrow returns close to the origin. Figures 4(a)-(c) show the phasor diagrams for three different absorption regions (C, D, E). In region C (corresponding to the high-loss, ENP region), the phasor arrow is significantly deflected away from the horizontal real axis. A high-loss film can induce a large phase angle in the complex reflection coefficient, and thus optical interference (or a closed loop in the phasor diagram) can occur even in ultra-thin films. The phase condition for this perfect absorption ($r = 0$) can be obtained from Eq. (5). From the numerator $r_{12} + r_{23}\exp(i2\beta) = 0$ and $r_{12} = -r_{21}$, we have $r_{23}/r_{21}\exp(i2\beta) = 1$. Thus, we have the following thin-film interference condition for perfect absorption [31],
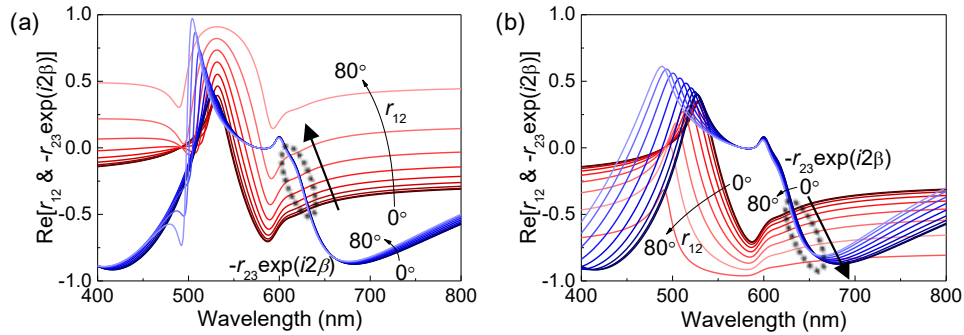
Fig. 4. (a)-(c) Partial reflected wave plots and (d)-(e) comparison of radiative and non-radiative damping for (a) Region C corresponding to ENP with $t = 50$ nm under p-polarization on the absorption map of Fig. 3(b). (b),(d) Region D corresponding to a high incidence-angle region with $t = 80$ nm under p-polarization on the absorption map of Fig. 2(a), and (c),(e) region E in the absorption map of Fig. 2(b) under s-polarization.

$$\varphi_{23} - \varphi_{21} + 2\varphi_{prop} = 2\pi m. \tag{6}$$

Here, ϕ_{23}, ϕ_{21} are the reflection phase shift, ϕ_{prop} is the propagation phase accumulation due to a single pass through the film, and m is an integer.

On contrary, in region D and E (corresponding to the low-loss and large incidence angle region for p- and s-polarization, respectively), the phasor arrows almost lie along the horizontal real axis. The final arrows return close to the origin, and thus reflection is minimized and near-perfect absorption is achieved again. Therefore, the phase condition in Eq. (6) should be still satisfied. However, in this case, we have from the relation $r_m = t_{12}t_{21}r_{23}{}^m r_{21}{}^{m-1}e^{2mi\beta}$,

$$\frac{r_2}{r_1} = \frac{r_3}{r_2} = \cdots = r_{23}r_{21}e^{2i\beta}. \tag{7}$$

Because the partial wave arrows are aligned linearly along the real axis, the phase of this term should be an integer multiple of 2π. Then, we obtain the following phase condition for low-loss perfect absorption:

$$\varphi_{23} + \varphi_{21} + 2\varphi_{prop} = 2\pi m. \tag{8}$$

This is in fact a Fabry-Perot resonance condition. Apparently, this condition seems in contradiction to Eq. (6) but, considering that $\phi_{21} \approx 0$ in a low-loss dielectric film, Eq. (8) becomes the same as Eq. (6) in the low-loss case. Therefore, we can understand that perfect absorption at a very large incidence angle occurs by coupling to a Fabry-Perot resonance. For much thicker films, we can also obtain higher-order resonances that have field nodes (i.e. zero electric-field points) inside the film (data not shown here). Similar thin-film interference and Fabry-Perot resonance can occur for air incidence too, as will be shown in the next section.
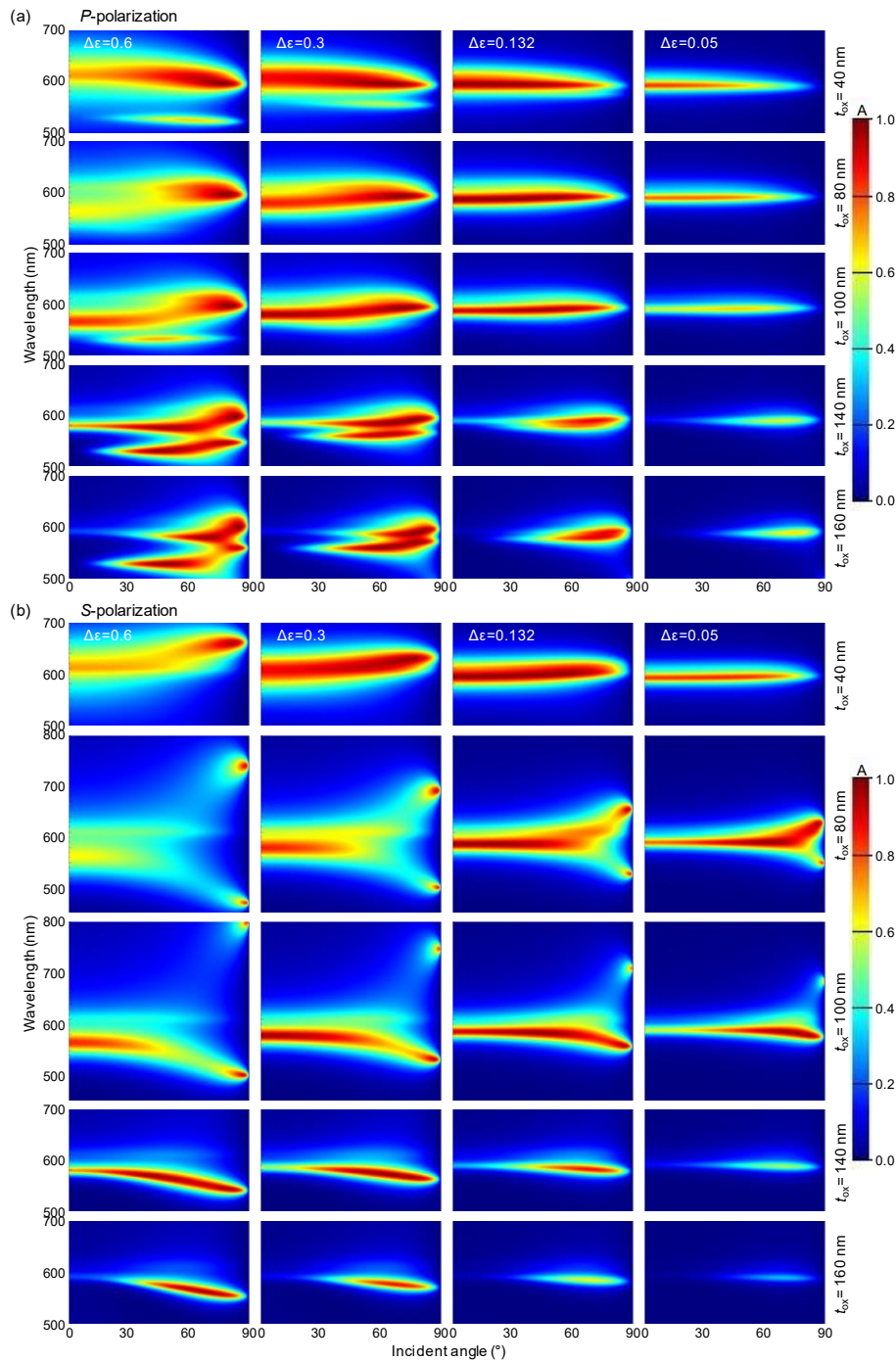
Fig. 5. Air-incidence absorption map as a function of wavelength and incidence angle for different $\Delta\varepsilon_{dye}$ and film thickness t (air/excitonic film/Ag back-reflector structure).

The near-unity absorption in the low-loss region can be explained further by comparing the radiative damping rate γ_{rad} (determined by the photon leakage rate from a resonance structure) and the nonradiative (or internal) damping rate γ_{nonrad} (determined by material losses). The

absorption spectrum $A(\omega)$ can be expressed as follows from temporal coupled mode theory [32],

$$A(\omega) = \frac{4\gamma_{rad}\gamma_{nonrad}}{(\omega - \omega_0)^2 + (\gamma_{rad} + \gamma_{nonrad})^2}, \tag{9}$$

where ω_0 is the resonant frequency. At the resonance frequency $\omega = \omega_0$, absorption reaches unity when $\gamma_{rad} = \gamma_{nonrad}$ (called critical coupling condition). We extracted the radiative and nonradiative damping rates by fitting a Lorentzian curve to the absorption spectra given in Fig. 2. Figures 4(d) and 4(e) compare the radiative and non-radiative damping rates as a function of incidence angle for region D and E. The radiative damping rate drops quickly as the incidence angle increases, while the nonradiative one is less sensitive to the incident angle. Therefore, two damping rates cross at 87.5° in region D and at 88.5° in region E. Owing to critical coupling to Fabry-Perot resonances, perfect absorption can occur even in the low-loss region.

5. Optical interactions in air incidence

Now we consider optical interactions in excitonic thin films when light is incident from air without a prism. We include a back reflector below the excitonic film (i.e., [air/excitonic film/silver] structure) and obtained the absorption spectra for *p*- and *s*-polarizations as shown in Figs. 5(a) and 5(b), respectively. Such a metal back mirror is often used in perfect absorbers to suppress light transmission. The film thickness is varied from 10 to 50 nm. For both polarizations, a strong absorption band appears near the ENP region. This strong absorption in the high-loss region can be understood as interference in lossy thin film as before. For *p*-polarization, we have an additional absorption band near the ENZ wavelength because of the excitation of Berreman modes. The Berreman mode is a leaky mode and thus it can be excited in air incidence. For $\Delta\varepsilon_{dye} = 0.6$, the Berreman mode dispersion curve is plotted as violet solid lines on the absorption maps. The absorption band matches the dispersion curve of Berreman modes well.
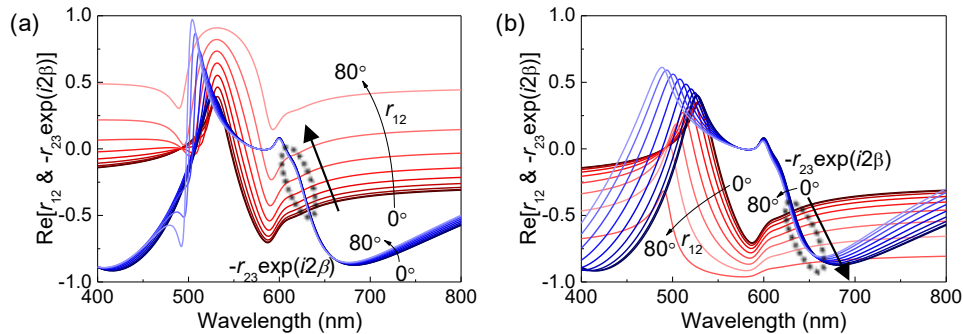

Fig. 6. The real part of r_{12} and $-r_{23}\exp(i2\beta)$, first and second term in the numerator of the reflection coefficient under (a) *p*-polarization and (b) *s*-polarization. The cross points of r_{12} and $-r_{23}\exp(i2\beta)$ in dotted circles correspond to the ENP region in Fig. 5(a) and (b). The angle dependence in the imaginary parts is much smaller, so it is not considered here.

In thicker films, the ENP absorption band slightly bends toward shorter wavelengths for *p*-polarization as the incident angle increases, while it bends to longer wavelengths for *s*-polarization. To understand this behavior, we compare relevant parameters [r_{12} and $r_{23}\exp(i2\beta)$] in the numerator of the reflection coefficient in Eq. (5). Figures 6(a) and 6(b) show r_{12} and -$r_{23}\exp(i2\beta)$ for gradually varying incidence angles under *p*- and *s*- polarizations, respectively. Around the ENP wavelength (near 600 nm), r_{12} has a strong incidence angle dependence, while -$r_{23}\exp(i2\beta)$ does not. The crossing points of these two curves become high absorption points (i.e. the numerator in Eq. (5) becomes small). We find that, for *p*-polarization [Fig. 6(a)], the

strong absorption point blueshifts as the incidence angle increases. For *s*-polarization [Fig. 6(b)], we see the opposite trend; it redshifts for larger incidence angles in agreement with the behavior shown in the TMM color map.
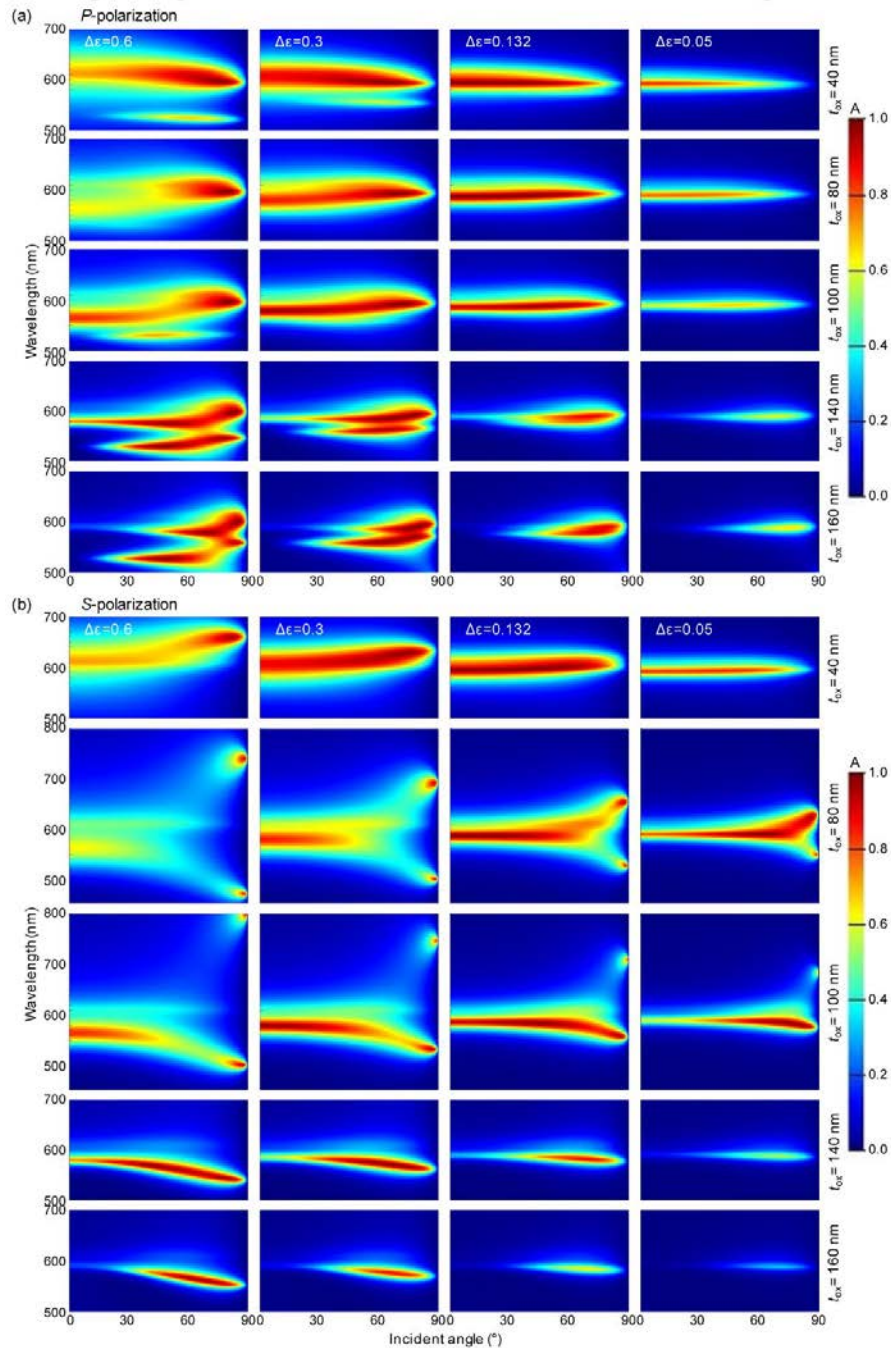

Fig. 7. Air-incidence absorption map as a function of wavelength and incidence angle for different $\Delta\varepsilon_{dye}$ and SiO$_2$ thickness t_{ox} (Air/excitonic film/SiO$_2$ spacer/Ag back-reflector structure). The excitonic film thickness is 30 nm.

We also consider a case that includes an additional phase-controller layer (i.e. SiO₂) between the excitonic film and silver. Figure 7 shows the absorption colormaps for the configuration [air/excitonic film/SiO₂/Ag]. Now we vary the oxide thickness from 40 nm to 160 nm, while the thickness of the excitonic film is fixed as 30 nm. We can notice that an absorption spectrum can be tailored further by controlling the phase-controller thickness. Various optical features appear in both high-loss and low-loss regions. Isolated, strong absorption points also appear at large incidence angles, similar to Fig. 2. These features can be again understood as thin film interferences and Fabry-Perot resonances in high-loss and low-loss regions.

6. Freespace impedance matching in excitonic thin films

Impedance matching to freespace can be also achieved in excitonic films because of the Lorentzian dispersion. Because the real part of the dielectric constants ($Re[\varepsilon]$) gradually changes across zero (from positive to negative), we could find a wavelength region where $Re[\varepsilon]$ becomes very close to 1. If the optical loss (or $Im[\varepsilon]$) of the film is small enough, the impedance matching condition can be satisfied around this point.
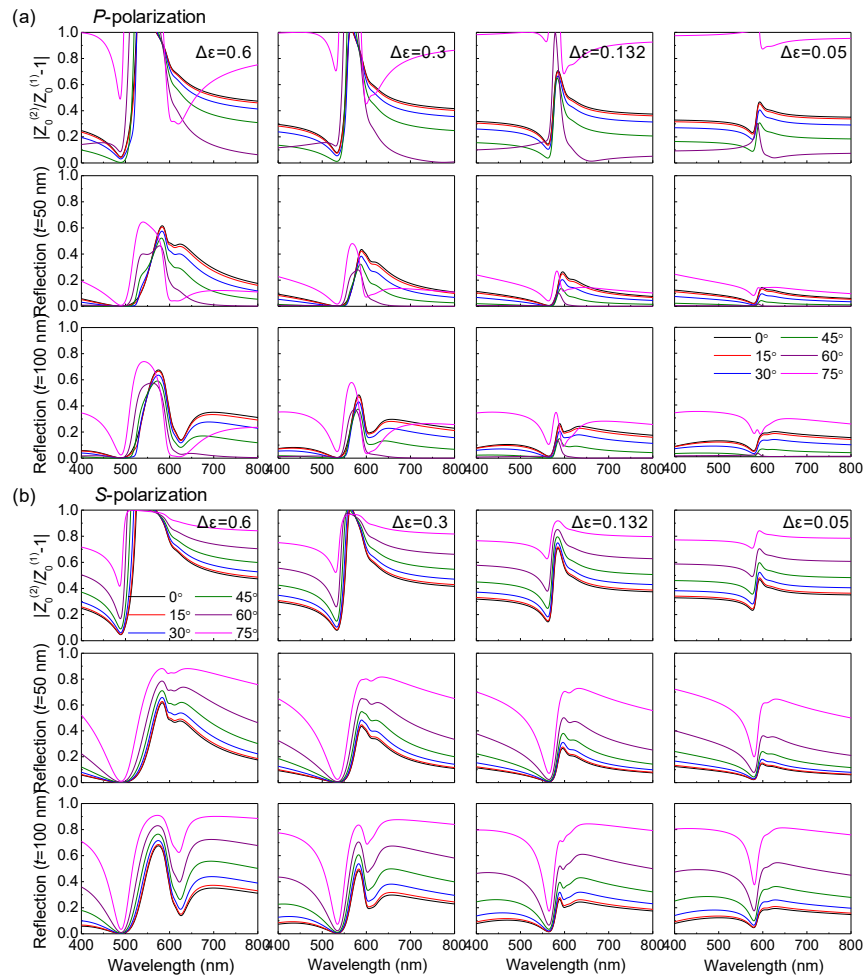

Fig. 8. (Top) Impedance spectra for a freestanding excitonic film ($\Delta\varepsilon_{dye}$: 0.6, 0.3, 0.132, 0.05). Reflection spectra for the freestanding excitonic film with thickness of 50 nm (middle) and 100 nm (bottom) for various incidence angles. (a) *p*-polarization and (b) *s*- polarization.

When the light is incident from medium 1 to 2, the characteristic impedance of the medium is defined as [33]

$$Z_0^{(1)}{}_p = \sqrt{\frac{\mu_1}{\varepsilon_1}} \cos\theta_1, \ Z_0^{(2)}{}_p = \sqrt{\frac{\mu_2}{\varepsilon_2}} \cos\theta_2, \ (\text{for } p-\text{polarization}), \quad (10.1)$$

$$Z_0^{(1)}{}_s = \sqrt{\frac{\mu_1}{\varepsilon_1}} \frac{1}{\cos\theta_1}, \ Z_0^{(2)}{}_s = \sqrt{\frac{\mu_2}{\varepsilon_2}} \frac{1}{\cos\theta_2} \ (\text{for } s-\text{polarization}), \quad (10.2)$$

where θ_1 and θ_2 are the incident and transmitted angles, respectively. For non-magnetic materials, $\mu = 1$. From Snell's law, we also have $\sqrt{\varepsilon_1} \sin\theta_1 = \sqrt{\varepsilon_2} \sin\theta_2$. Therefore, the impedance matching condition, $Z_0^{(1)} = Z_0^{(2)}$, can be expressed as following,

$$\frac{Z_0^{(2)}{}_p}{Z_0^{(1)}{}_p} = \sqrt{\frac{\varepsilon_1}{\varepsilon_2}} \frac{\cos\theta_2}{\cos\theta_1} = 1 \ (\text{for } p-\text{polarization}), \quad (11.1)$$

$$\frac{Z_0^{(2)}{}_s}{Z_0^{(1)}{}_s} = \sqrt{\frac{\varepsilon_1}{\varepsilon_2}} \frac{\cos\theta_1}{\cos\theta_2} = 1 \ (\text{for } s-\text{polarization}). \quad (11.2)$$

The medium 1 and 2 are air and the excitonic film in our case. From the Fresnel equation, we can notice that this impedance matching should result in the suppression of reflection:

$$r = \frac{Z_0^{(2)} - Z_0^{(1)}}{Z_0^{(2)} + Z_0^{(1)}} = \frac{Z_0^{(2)}/Z_0^{(1)} - 1}{Z_0^{(2)}/Z_0^{(1)} + 1}. \quad (12)$$

The calculated characteristic impedances with various incidence angles under p- and s-polarizations are presented in the top panel in Figs. 8(a) and 8(b), respectively. For easy comparison with reflection spectra, $|Z_0^{(2)}/Z_0^{(1)} - 1|$ are presented for several incidence angles instead of the respective values $Z_0^{(2)}$ and $Z_0^{(1)}$. For $\Delta\varepsilon_{\text{dye}} = 0.6$ under both p- and s-polarizations, $|Z_0^{(2)}/Z_0^{(1)} - 1|$ are close to zero at 492 nm. Only for very large incidence angles, $|Z_0^{(2)}/Z_0^{(1)} - 1|$ becomes bigger. Therefore, one can expect that reflection should be minimized at this wavelength because of freespace impedance matching. As $\Delta\varepsilon_{\text{dye}}$ decreases, the impedance matching point redshifts. Such impedance matching curves are compared with reflection spectra. The middle and bottom panels in Figs. 8(a) and 8(b) show the reflection spectra under the p- and s-polarizations of incident light for 50 nm and 100 nm thick films in freespace (i.e. assuming a freestanding film without a substrate). As expected, for $\Delta\varepsilon_{\text{dye}} = 0.6$, we have near-zero reflection at 492 nm for both p- and s-polarizations. At longer wavelengths (beyond 600 nm), we also have near-zero reflection at the Brewster angle (~60°). This occurs over a broad wavelength range and we can confirm that it occurs only for the p-polarization of incident light.

7. Conclusion

In summary, we have investigated surface bound modes and optical interactions in organic excitonic films (such as J-aggregate-doped polymer films). Excitonic films can exhibit an optically metallic response for high-enough dye concentrations. By varying the dye concentration in a polymer film, we can realize both optically metallic and non-metallic films. Excitonic films have various optical features in the visible region because of sharp Lorentzian dispersions; excitonic SPs, ENZ (Re[ε] ~0), ENP (Im[ε] ~peak), and freespace impedance matching ($Z_0^{(2)}/Z_0^{(1)}$ ~1). We performed systematic studies by gradually varying the dye concentration and film thickness. Our work shows that optical modes and interferences can be significantly controlled in organic excitonic films by adjusting the dye concentration in a polymer matrix and the film thickness. Because organic films are commonly prepared by a solution process, both dye concentration and film thickness can be easily controlled. Therefore,

our work suggests an easy and very effective method for nanophotonic studies in the visible region. Moreover, as far as we know, there were no studies on ENZ modes in natural materials in the visible region. There have been studies on ENZ modes in doped semiconductors and polar dielectric materials, but they were all performed in the infrared region. Our work shows that ENZ modes can be excited in the visible region using organic excitonic films. Especially, we showed that incident light can couple to either excitonic SP modes or ENZ modes depending on the film thickness. We also clarified the optical mode responsible for absorption resonances in the low-loss region. We found that strong absorption resonances in the low-loss, large-incidence-angle region satisfy the Fabry-Perot resonance condition. Finally, we discussed the freespace impedance matching that can be achieved because of the Lorentzian dispersion. This impedance matching is interesting because it can occur in planar, spincoated films without further nanoscale patterning.

Strong light absorption in the high-loss and low-loss regimes with tailored spectral and angular responses could be potentially useful for photodetectors, energy harvesting devices, fluorescence-based optical sensors, and color filters. ENZ modes in the visible region could be also interesting for nonlinear optical enhancement and active devices. Planar, organic excitonic films can be easily prepared by spincoating over a large area and can show various optical features in the visible region without complicated nanopatterning. Therefore, they provide a simple and cost-effective solution for many nanophotonic applications in the visible region.

Funding